

Effects of Ion Adsorption on Graphene Oxide Films and Interfacial Water Structure: A Molecular-Scale Description

Amanda J. Carr¹, Raju Kumal¹, Wei Bu², Ahmet Uysal^{1}*

¹Chemical Sciences and Engineering Division, Argonne National Laboratory, Lemont, IL 60439,
United States

²NSF's ChemMatCARS, The University of Chicago, Chicago, IL 60637, United States

*Corresponding author: ahmet@anl.gov

KEYWORDS: ion adsorption, graphene oxide, air-water interface, x-ray reflectivity, x-ray
fluorescence near total reflection, sum frequency generation spectroscopy

ABSTRACT

Graphene oxide is a promising, emerging separation material, as it is durable, dispersible in water, and has naturally forming functional groups. Bulk studies using graphene oxide flakes have demonstrated impressive metal adsorption. However, little interfacial information about metal adsorption on graphene oxide is available and inferring interfacial structure from bulk experiments is usually not possible. A mechanistic understanding of ion adsorption on graphene oxide films is critical toward advanced separations, including improved sorption efficiency and membrane regeneration. In this paper, we study metal ion adsorption onto graphene oxide films formed at the air/water interface using x-ray reflectivity (XR), x-ray fluorescence near total reflection (XFNTR), and vibrational sum frequency generation spectroscopy (SFG). These interface-specific techniques provide the electron density profile normal to the interface, number of adsorbed ions, and information about the orientational ordering and hydrogen-bonding network of interfacial water, respectively. Via XFNTR and SFG, we find that trivalent yttrium ions preferentially adsorb to graphene oxide compared to divalent strontium and monovalent cesium ions. These trivalent ions affect the graphene oxide film structure significantly. The SFG data show that at least two different interfacial water populations can be described, based on their hydrogen bonding strength, and the adsorbed ions affect these populations differently. We demonstrate that ion adsorption onto graphene oxide is more complex than simple electrostatics and requires thorough interfacial investigation. These results pave the way toward improved soft-scaffold graphene oxide membranes and applications and provide fundamental information about the ion adsorption mechanism at the interface.

INTRODUCTION

Graphene oxide (GO), the oxidized analogue of sp^2 -hybridized graphene, is a promising, emerging separations material that is well-suited for metal ion adsorption.¹ GO flakes are typically synthesized through chemical exfoliation of graphite.² In general, GO flakes have both hydrophilic edges and hydrophobic basal planes,³ meaning they are dispersible in water, durable,^{4,5} and surface active.⁶⁻⁷ The final chemical and physical properties of the flakes strongly depend on the synthetic route⁸⁻⁹ with minor changes affecting average flake size^{7, 10-11} and polydispersity,⁴ as well as the number density, placement, and type of oxygen-based functional groups.^{7, 12} Consequently, adsorption studies using GO-based separation membranes have demonstrated a range of sorption capabilities, likely linked to small changes in GO preparation and final structure.⁸ . Despite the widespread applicability of GO, there is limited fundamental molecular adsorption information. A molecular-level understanding of interfacial ion adsorption is critical toward developing GO as a useful membrane material, with improvements including increased sorption efficiency and membrane regeneration.

GO as a filtration medium has shown useful results for both gas¹³ and liquid applications.¹⁴ In these systems, the diffusive species navigate through micro-channels formed in between dried GO flakes,¹⁵⁻¹⁶ the size of which can be successively manipulated via cross-linking flakes with ions and polymers^{4, 17-18} to affect permeability. Adsorption studies using similar densely-packed GO films have demonstrated permeation and separation success with small monovalent ions¹⁹ and alcohols.²⁰ Pure GO membranes swell upon addition of water, which can affect filtration by changing inter-flake spacing and micro-channel sizes.¹⁶ To provide additional structural support, separations with GO composites have been investigated, including cellulose,¹¹ and alginate and

chitosan,²¹ among other polymers.²² These applied studies report varying sorption success without specifically investigating the molecular-scale details.

Bulk adsorption studies utilizing GO in model aqueous systems have probed the applicability of GO in a range of separation efforts including: cesium,²³⁻²⁵ strontium,^{23, 26-27} technetium,²⁷ lead,²⁸ europium,^{25, 27, 29-31} thorium,^{27, 32-33} uranium,^{25, 27, 29, 31-32, 34-36} neptunium,^{27, 32} plutonium,²⁷ and americium.^{25, 27, 31} Few studies have also considered adsorption of other molecules on GO³⁷ and adsorption of GO on other materials.³⁸⁻³⁹ Bulk techniques, namely FTIR, Raman, UV-vis, and x-ray photoelectron spectroscopy (XPS), have identified varied adsorbed metal-GO binding, ranging from likely electrostatics^{23, 25} to specific binding with sulfur- and oxygen-based groups,^{25, 32, 40} although the exact binding mechanisms remain unknown. Computational efforts have supported these findings,⁴¹⁻⁴² mainly with surface complexation models.^{29, 31-32} However, a large gap between computational and experimental agreement still exists.

The amphiphilic and surface-active nature of GO has spurred interfacial experiments as well. Langmuir-Blodgett films prepared from GO dispersions successively spread on aqueous subphases have confirmed surface activity.⁴³⁻⁴⁶ Although GO is not a traditional surfactant,⁸ it can stabilize water-oil emulsions^{7, 47} with limited studies considering the oil-water interface specifically.⁴⁸ The air-water interface is particularly relevant to separation efforts but can be difficult to isolate from the bulk. Synchrotron x-ray reflectivity (XR) measurements are well-suited for interfacial efforts and can provide the total electron density profile (EDP) perpendicular to the air-water interface. Bonatout et al. probed interfacial GO flakes on plain water, using XR, and found spontaneous bilayer formation at low surface pressures.⁴⁹

In a different approach, David et al. used vibrational sum frequency generation (SFG) spectroscopy to examine the GO-water interface formed in between GO films spin-coated on

sapphire and plain water.⁵⁰ SFG is a second-order, non-linear technique where an input visible and IR overlap spatially and temporally on a sample surface to generate a new frequency (ω) equal to the sum of the input frequencies, i.e. $\omega_{SFG} = \omega_{vis} + \omega_{IR}$. This process is forbidden in centrosymmetric within the electric dipole approximation, thus eliminating bulk phase contributions.⁵¹⁻⁵³ David et al. reported both experimental and computational SFG data and demonstrated clear changes in the local water network for GO samples with different degrees of oxidation, which was further investigated in another computational work.⁵⁴ Neither study considered the effects of ion adsorption on the local water network or experimentally measure the soft air-water interface.

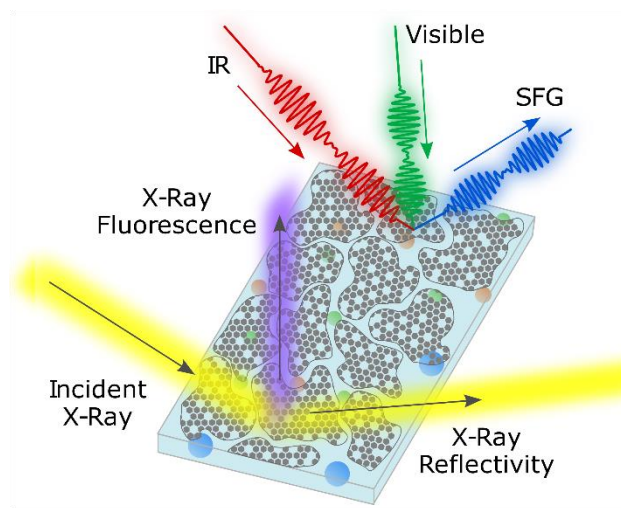


Figure 1. Experimental cartoon showing interfacial x-ray reflectivity (XR), x-ray fluorescence near total reflection (XFNTR), and vibrational sum frequency generation spectroscopy (SFG) measurements on the air-water interface. GO flakes are pinned on a dilute aqueous subphase. XR measurements provide the total electron density profile perpendicular to the interface. XFNTR yields the quantitative adsorbed ion density. SFG measures changes in the local water network near the interface as induced by metal ion adsorption.

In this paper, we examine metal ion adsorption onto GO thin films formed at the air-water interface using XR, x-ray fluorescence near total reflectivity (XFNTR), and SFG spectroscopy (Figure 1). These self-formed thin films exist without additional structural support and can provide information about GO behavior in soft-scaffold applications. Our XR measurements provide the nanoscale structure of the GO thin films. XFNTR is an interfacial-specific fluorescence technique that provides the quantitative adsorbed metal ion density by collecting x-ray fluorescence signal as a function of inverse momentum transfer Q_z around the interfacial critical angle Q_c . SFG data provide molecular-scale information about the local water network, which is directly affected by ion adsorption. Together, these techniques provide nanoscale information about ion adsorption onto soft-scaffold GO films. We find via XFNTR and SFG that trivalent yttrium ions (Y^{3+}) adsorb more strongly compared to divalent strontium (Sr^{2+}) and monovalent cesium (Cs^{1+}) ions. XR reveals a relatively complex GO structure after yttrium adsorption. Y^{3+} also disrupt the hydrogen bonding network present, as evidenced from SFG. We speculate yttrium interacts with the varied functional groups present on the hydrophilic edges of the GO flakes, meaning ion adsorption to GO is more complex than simple electrostatic attraction.

EXPERIMENTAL

Materials and sample preparation

All chemicals were purchased from Sigma Aldrich and used as is. We prepared 20 mM and 0.05 mM solutions using cesium (I) chloride ($CsCl$, $\geq 99.999\%$ trace metals basis), strontium (II) chloride hexahydrate ($SrCl_2 \cdot 6H_2O$, 99.995% trace metals basis), yttrium (III) chloride hexahydrate ($YCl_3 \cdot 6H_2O$, 99.99% purity), and ultrapure water with a resistivity of 18.2 $M\Omega \cdot cm$ (Millipore, Synergy Water Purification System). To make the graphene oxide samples, we diluted commercially available graphene oxide (GO, 4-10% edge oxidized, 1 mg/mL, dispersed in water)

with 1 part GO and 5 parts methanol (99.8% anhydrous), and sequentially filtered with 1.2, 0.45, and 0.2 μm syringe filters. GO flake size was measured using dynamic light scattering (ZetaSizer Nano ZS).

In general, we prepared films by slowly spreading a small amount of GO from a 1 mL glass Hamilton syringe over the desired aqueous subphase. We monitored the surface pressure with a pressure sensor (Nima) equipped with a chromatography paper Wilhelmy plate. For SFG experiments, monolayers were prepared in a 60 x 20 mm² flat-form polytetrafluoroethylene dish. For x-ray experiments and pressure-area isotherms (Supporting Information), films were prepared using a Langmuir trough with a single barrier. We made Langmuir-Blodgett GO films by preparing a film on a Langmuir trough with two barriers and transferring the film onto clean Si/SiO₂ wafers. XPS (Thermo Scientific ESCALAB 250Xi) was completed on Langmuir-Blodgett GO films (Supporting Information).

Vibrational sum frequency generation spectroscopy experiments

SFG experiments were carried out using an EKSPLA laser system, described in detail elsewhere.⁵⁵⁻⁵⁸ Briefly, an amplified Nd:YAG laser system produces 29 ps pulses with 28 mJ energy centered at 1064 nm at a repetition rate of 50 Hz. A harmonic unit and a second harmonic crystal split the 1064 nm laser into two beams of 532 nm. One of these 532 nm beams and the 1064 nm beam are used to generate a narrowband IR pulse, tunable from 1000 – 4000 cm⁻¹, via an optical parametric generator and difference frequency generation. The other 532 nm beam is then overlapped spatially and temporally with the narrowband IR pulse at the sample surface to generate the sum frequency signal. A Glan polarizer adjusts the polarization of the final 532 nm beam and SFG signal while computer controlled motorized mirrors adjust the IR beam polarization. A photomultiplier tube connected to a monochromator detects the final SFG signal.

The SFG spectrometer uses a reflection geometry where the incident angles of the 532 nm and IR beams are 60° and 55°, respectively, to the surface normal. We attenuate the visible light to 200 μJ and maintain the IR light at 100 μJ for all measurements. Each spectrum is collected with a 4 cm⁻¹ step from 3000 – 3800 cm⁻¹. Each datum point is an average of 300 laser shots. We collect spectra in various polarization combinations and normalize the data to z-cut quartz. The surface pressure for each experiment was 20-22 mN/m and samples were measured at room temperature.

The collected SFG signal (I_{SFG}) is proportional to the product of the incident beams intensities and the square of the effective second order non-linear susceptibility $\chi^{(2)}$ of the interface i.e.

$$I_{SFG} \propto |\chi^{(2)}|^2 I_{Vis} I_{IR} \quad (1)$$

where

$$|\chi^{(2)}|^2 \propto \left| \chi_{NR}^{(2)} + \sum_n \frac{A_n}{\omega_{IR} - \omega_n + i\Gamma_n} \right|^2. \quad (2)$$

Here, $\chi_{NR}^{(2)}$ is the non-resonant component of $\chi^{(2)}$, A_n is the resonant amplitude, ω_n is the resonant frequency, and Γ_n is the dampening constant that determines the peak width, each of the n^{th} vibrational mode while ω_{IR} is the IR beam frequency. For a charged interface, the static electric field allows some bulk contribution to the SFG signal, commonly called the $\chi^{(3)}$ effect.⁵⁹⁻⁶¹ For these systems,

$$|\chi^{(2)}|^2 \propto \left| \chi_{NR}^{(2)} + \sum_n \frac{A_n}{\omega_{IR} - \omega_n + i\Gamma_n} e^{i\gamma_n} + \frac{\kappa}{\sqrt{\kappa^2 + \Delta\kappa_z^2}} e^{i\varphi} \chi^{(3)} \Phi_0 \right|^2 \quad (3)$$

where γ is the phase angle of the resonant component of $\chi^{(2)}$, κ is the inverse Debye screening length, $\Delta\kappa_z$ is the inverse SFG coherence length, φ is the $\chi^{(3)}$ phase angle, and Φ_0 is the surface potential. Additional details are provided elsewhere.⁵⁹

For the bimodal water region, we fitted SFG data with two Lorentzian peak functions via the sum of least-squares using Equation 3. $\chi_{NR}^{(2)}$ was fitted to plain water data and held constant for other measured concentrations. Peak width and frequency were fitted as global variables for all data sets – only the measured resonance amplitudes for each χ component were fitted individually for each considered concentration.

Synchrotron x-ray experiments

X-ray experiments were conducted at sector 15-ID-C (NSF’s ChemMatCARS) of the Advanced Photon Source at Argonne National Laboratory. We collected XR and XFNR data using an incident x-ray energy of 18.3 keV. Two motorized slits set the incident beam size to 2 mm horizontally and 0.02 mm vertically. XR signal was detected on a Pilatus 200 K area detector. A Vortex-60EX multi cathode energy dispersive x-ray detector, placed perpendicularly 10 mm above the liquid surface, recorded fluorescence signal. Films were prepared on a Langmuir trough inside a chamber, which was purged with He to reduce background scattering and beam damage.

X-ray reflectivity measurements

We recorded specular x-ray reflectivity as a function of inverse transfer momentum $Q_z = (4\pi/\lambda) \sin(2\theta/2)$ where λ is the wavelength and θ is the incident angle. The sample was shifted periodically to avoid beam damage effects. Models using different numbers of slabs were used, as detailed in the Discussion. We fit the collected XR data to calculated curves using the sum of least-squares via a Parratt formalism to determine slab thickness, roughness, and electron density

(Supporting Information). For models with multiple slabs, the roughness values at all interfaces are dominated by surface capillary waves and were consequently forced to be equal.⁶²⁻⁶³

X-ray fluorescence near total reflection measurements

The x-ray fluorescence intensities⁶⁴ of the L_{a2} (4.287 keV) for Cs, K_{a1} (14.165 keV) for Sr, and K_{a1} (14.958 keV) for Y were collected as a function of Q_z around the critical angle. The beam footprint was always larger than the detector area, meaning only the depth of the illuminated volume varies with incident angle. The total illuminated volume was calculated via the beam dimensions, as described elsewhere,⁶⁵ and used to calculate XFNR data via sum of least-squares.⁶⁵

RESULTS AND DISCUSSION

Y³⁺ adsorption to graphene oxide

We first investigated ion adsorption to GO films spread on high and low concentration YCl_3 subphases, using XFNR (Figure 2). This surface-sensitive technique is the most direct way to determine the number of ions adsorbed to the interface. XFNR measures x-ray fluorescence as a function of inverse momentum transfer Q_z near the critical angle Q_c , which is $\sim 0.0217 \text{ \AA}^{-1}$ for these systems. Because we do not see interfacial signal for subphases without a GO film, we reasonably posit that metal ions pinned to the interface and detected with XFNR are adsorbing to the GO. For a 20 mM YCl_3 subphase and a GO film compressed to 20 mN/m, we found 1 adsorbed Y^{3+} per $149 \pm 19 \text{ \AA}^2$. Signal intensity measured at $Q < Q_c$ shows intensity primarily from ions within the interfacial region, as the x-rays undergo total external reflection,^{62, 65-66} and only evanescent waves penetrate a few nanometers of the liquid. Data from this region are highlighted in the Figure 2 inset. Signal intensity at the high Q_z values were larger than predicted by our model. We speculate our GO samples are not smooth monolayers at the air-water interface and instead form crumpled,

multilayer structures,⁴⁹ meaning excess Y^{3+} ions can exist, as discussed in detail later. This effect is even more noticeable for GO compressed to 30 mN/m on a 20 mM YCl_3 subphase (Supporting Information).

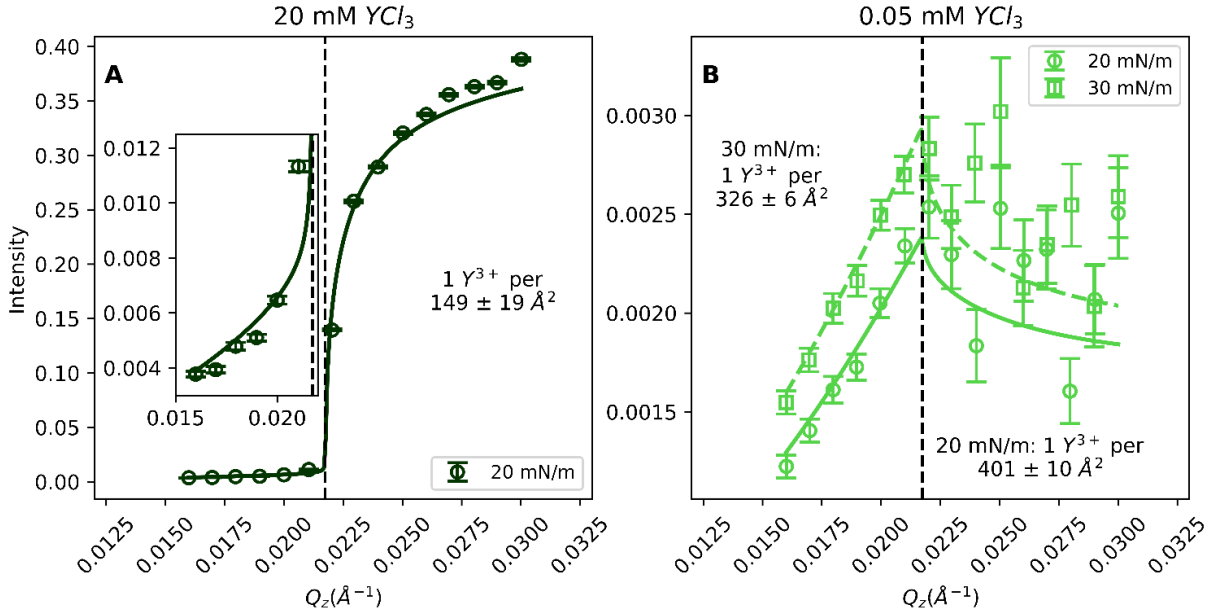


Figure 2. Surface-sensitive x-ray fluorescence near total reflection (XFNTR) intensity and fits (lines) plotted over inverse momentum Q_z for graphene oxide films spread on 20 mM (A) and 0.05 mM (B) YCl_3 . The monolayer was compressed to 20 mN/m for the 20 mM subphase, and to 20 (circles) and 30 (squares) mN/m for the 0.05 mM subphase. Error bars are derived from counting statistics.

We next considered dilute YCl_3 subphases to understand adsorption behavior in an unsaturated system. Figure 3 shows XFNTR data for GO film compressed to 20 mN/m and 30 mN/m spread on 0.05 mM YCl_3 . With a lower subphase concentration, we see less bulk signal above Q_c , as the signal from the surface decreases with increasing Q_z , and the bulk concentration is below the limit where their signal can reach to the detector. The noise in the bulk region data is probably due to the small number of ions above the surface due to the crumbled GO structure.

We focus on the data below Q_c to understand ion adsorption to the GO. For GO compressed to 20 mN/m, we obtain an ion density of 1 ion per $401 \pm 10 \text{ \AA}^2$ while for GO compressed to 30 mN/m, we find an ion density of 1 ion per $326 \pm 6 \text{ \AA}^2$. The increase in adsorbed ion density for the higher surface compression and overall increase in intensity implies more ions per area are adsorbed to the film. A higher surface pressure compression means more GO is occupying the available film space. Thus, more ions can adsorb and increase the surface density.

Notably, GO dispersions have varied chemical and physical properties depending on the preparation method, which strongly affects film behavior and subsequent ion adsorption. We are currently investigating these effects in detail, which will be reported in another publication. In this work, we exfoliate commercial GO dispersions with methanol and use filtration to isolate GO flakes. XPS analysis of Langmuir-Blodgett thin-film GO samples^{7, 44} (Supporting Information) provides a rough density estimate of ~ 1 carboxyl group per 60 \AA^2 and ~ 1 epoxy group per 30 \AA^2 . These values represent the higher limit of possible available oxygen groups. Evidently, we observe less adsorbed Y^{3+} than available sites, meaning the theoretical experimental binding capacity for GO is much higher. In a recent study, we demonstrate enhanced Y^{3+} adsorption onto plain electrified graphene with approximately 1 Y^{3+} per 11 \AA^2 .⁶⁷ That system lacks functional groups and demonstrates electrostatic adsorption without disrupting the hydration shell of Y^{3+} . The current GO system demonstrated more complicated adsorption with partial or full dehydration of the adsorbed ions. We speculate one can tune the degree of functionalization across the graphene-derivative to maximize adsorbed ion loading.

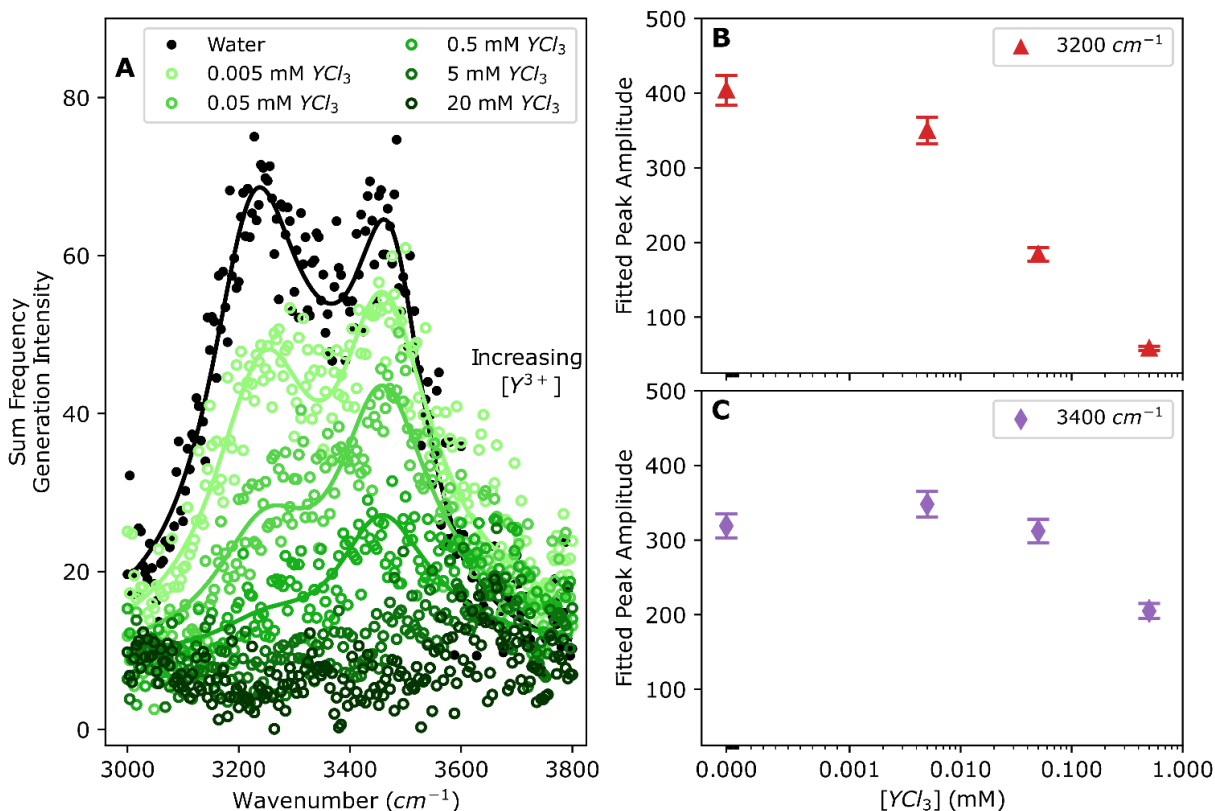


Figure 3. Sum frequency generation spectroscopy intensity and fits (solid lines) plotted over wavelength for the water region of a graphene oxide film spread over YCl_3 subphases of varying concentration (colors) (A). The surface pressure of the GO was 20 mN/m. Typical water band signal is also shown (black). Fitted $\chi^{(2)}$ peak amplitudes plotted over subphase concentration for the 3200 (B) and 3400 (C) cm^{-1} water signal features.

Interfacial water structure near graphene oxide

We investigated molecular water and ion behavior near GO using SFG, a non-linear interfacial-specific vibrational technique. We examined the -OH stretch of the water region for our GO films at 20 mN/m on different YCl_3 subphases using SSP (SF, visible, and IR) polarization (Figure 3A). GO on plain water shows a bimodal peak at maximum intensity with centers at approximately 3200 and 3400 cm^{-1} , assigned to strongly and weakly hydrogen bonded -OH stretches of interfacial

water, respectively.⁶⁸⁻⁶⁹ The absence of signal near 3700 cm⁻¹ suggests there are no water molecules with free-dangling -OH bonds pointing upward away from the subphase, meaning a uniform film is present.^{60, 70} XPS results show primarily carbon and oxygen signal with some sulfur contamination (Supporting Information)⁷¹ and a 5.21 carbon : oxygen ratio, meaning our GO films are primarily carbon and lack a significant amount of oxygen functional groups. Accordingly, our SFG data agree with other published experimental SFG data on a thermally reduced GO film spin-coated on sapphire.⁵⁰ Our GO films are self-assembled at the interface without a solid substrate, and can provide adsorption information relevant to soft-scaffold separation systems.

Signal for 0.005 mM YCl₃ shows the water peaks but the absolute intensities are lower. The decrease in intensities can have two main reasons, both resulting from the ion adsorption to the monolayer.^{55, 72-73} Ion adsorption can screen the surface charge of the interfacial film thus effectively reducing the electric field normal to the liquid surface facing down into the subphase. These screening effects reduce water molecule alignment and decrease SFG signal. This is usually referred as the $\chi^{(3)}$ effect. Ions can also directly disrupt the orientational ordering of the interfacial water molecules, typically within the first two monolayers of the interface, which directly affect the $\chi^{(2)}$. As we continue to increase the subphase concentration, the water peak intensities decrease. Both peaks are completely suppressed for the 5 and 20 mM data, indicating that above a certain ion concentration the interfacial water structure is completely lost. The local water network has been significantly disrupted due to the adsorbed Y³⁺ and no water signal is detected. Hong et al. reported a similar observation using a different GO spread on a NaCl subphase and state the addition of a salt in the subphase decreased SFG intensity by diminishing the $\chi^{(3)}$ effect.⁷⁴

Interestingly, the relative water band intensities also change with increasing subphase concentration. To highlight these changes in water peak intensity as a function of subphase

concentration, we fitted the SFG signal to Equation 3, which considers the $\chi^{(3)}$ effect explicitly. The $\chi^{(2)}$ peak amplitudes for the 3200 and 3400 cm^{-1} bands plotted over YCl_3 concentration are presented in Figure 3B-C. Additional fit parameters are given in Tables S1 and S2. Data were also fitted using Equation 2, without the explicit $\chi^{(3)}$ term, and a similar trend was observed (not shown). Evidently, the fitted amplitude for the 3200 cm^{-1} feature rapidly decreases with increasing YCl_3 concentration while the amplitude of the 3400 cm^{-1} peak remains relatively unchanged. Because we explicitly include $\chi^{(3)}$ within our fitting process, these decreases in amplitude terms are not from changes to the local electric field as induced by shielding from the adsorbed ions. We speculate Y^{3+} adsorption is not simply electrostatic, as features of the water network change differently. In the absence of metal ions, water can form strong hydrogen bonds with the carboxyl and hydroxyl groups of the GO, which significantly contributes to the 3200 cm^{-1} peak intensity. As metal ions adsorb and disrupt the local water network, we see a large decrease in this peak intensity. We posit the 3400 cm^{-1} band stems from weakly hydrogen bonded water molecules adjacent to the GO or perhaps in between the GO layers, the structure of which will be discussed later. The amplitudes for the 3400 cm^{-1} do not significantly change with subphase concentration, which suggests these weakly hydrogen bonded water molecules do not change. At concentrations above 5 mM, this band disappears because the adsorbed Y^{3+} have sufficiently disrupted local water organization, and possibly have penetrated the GO layered structure thus affecting any water in between the layers. We present these arguments as first order approximations and are currently investigating water orientation and organization near GO films with molecular dynamic simulations, which can reveal important details.^{50, 75}

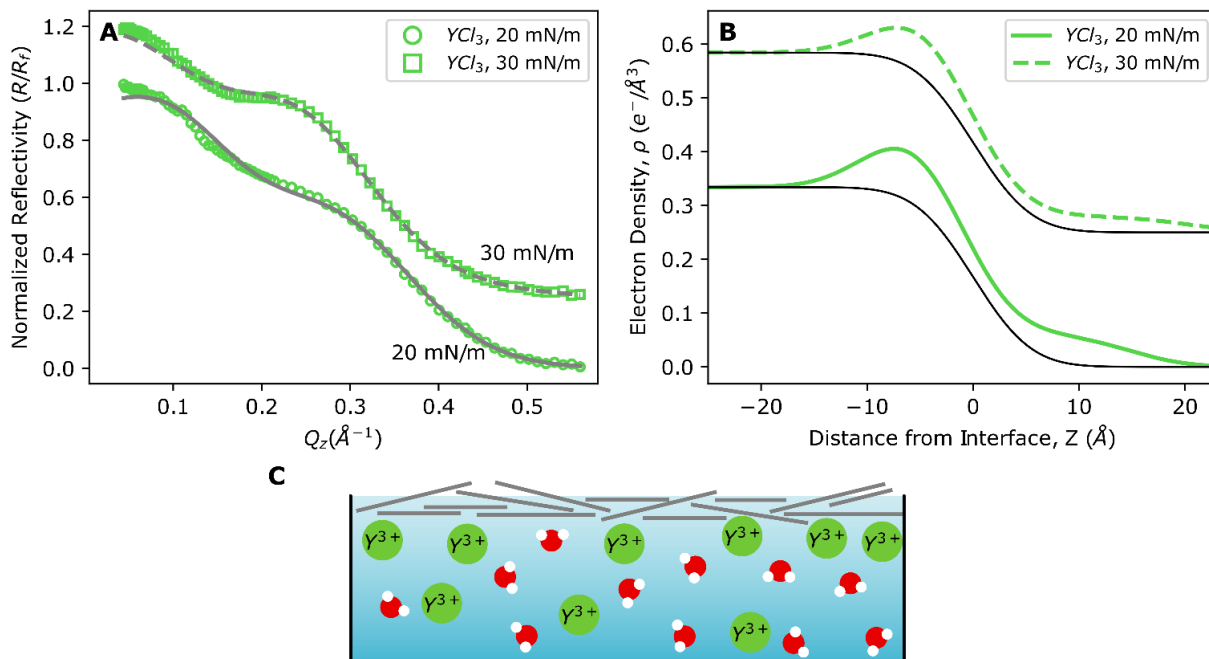


Figure 4. Normalized x-ray reflectivity plotted over vertical momentum transfer, Q_z for graphene oxide films compressed to 20 (circles) and 30 (squares) mN/m spread on 0.05 mM YCl_3 subphases. Data were fit using a 2-slab model (lines). 30 mN/m data are vertically offset for clarity. Calculated electron density from fitted reflectivity data plotted over distance from interface Z (B) for graphene oxide monolayers compressed to 20 (solid line) and 30 (dashed line) mN/m spread on 0.05 mM YCl_3 subphases. An ideal interface electron density profile is included (black). 30 mN/m data are vertically offset by $+0.25 e^-/\text{\AA}^3$ for clarity. Proposed interfacial structure (not to the scale) (C).

Interfacial graphene oxide structure after Y^{3+} adsorption

Taken together, the XFNR and SFG analysis show Y^{3+} adsorption onto GO particles assembled at the air-water interface. XR studies complement these observations by providing the molecular-scale structure of GO films (Figure 4). XR data collected for GO spread on a dilute 0.05 mM YCl_3 subphase and compressed to 20 mN/m show a small dip around $Q = 0.18 \text{\AA}^{-1}$ and broad peak near $Q = 0.28 \text{\AA}^{-1}$. The 30 mN/m XR data have a higher intensity overall and show a distinct dip in

reflectivity around $Q = 0.16 \text{ \AA}^{-1}$ and a larger broad peak around $Q = 0.24 \text{ \AA}^{-1}$. These features imply the film on the liquid surface is not a simple layer in Z -direction and consequently, requires a 2-slab model to fit the data and obtain the electron density profile (Figure 4B). A slab containing a lower electron density was necessary to fit the dips in the XR data. Since GO electron density is close to the water electron density and capillary oscillations smear the profile. Nevertheless, it is possible to capture the main features of the GO film. We report the fitted electron densities and thicknesses in the supporting information.

The resulting electron density profiles are plotted over Z where $Z = 0 \text{ \AA}$ is loosely the top of the bulk liquid and Z increases into the air. Both the 20 and 30 mN/m data show an expected increase in density around $Z = -5 \text{ \AA}$, corresponding to the film sitting on a liquid interface, with an enhanced electron density near $Z = -10 \text{ \AA}$. For the 20 mN/m sample, this enhancement has an electron density of $0.52 e/\text{\AA}^3$ and a thickness of 6.77 \AA . The 30 mN/m sample electron density fit gives a slightly higher electron density of $0.54 e/\text{\AA}^3$ and a slightly smaller thickness of 5.33 \AA , also at $Z = -10 \text{ \AA}$. We posit these high electron density slabs represent the interfacial region closer to the bulk solution that contains adsorbed Y^{3+} and a crumpled, multilayer GO film (Figure 4C).

Y^{3+} can interact via electrostatics with any available functional groups on the GO. These results can be compared to the bulk GO studies of Am (III) and Eu (III), which have found metal hydroxyl, epoxy, and carboxylate interactions.²⁵ As Y^{3+} adsorb to the GO, the ions have enough charge to attract deprotonated oxygen-containing and sulfur contaminate groups on the GO. This rearrangement forces the GO flakes to tilt and generates a rough, crumpled GO film that can, in addition to the adsorbed ions, reflect more signal and be detected using XR.⁴⁷ There is little difference in between the 20 and 30 mN/m structures, meaning the GO interfacial structure does not change significantly with increasing surface pressure. Based on the obtained pressure-area

isotherms (Supporting Information), the GO monolayer is likely in the same condensed phase at both 20 and 30 mN/m where GO sheets are touching and overlapping to create a multilayer structure.^{44, 46, 49} The measured structures at both pressures are mechanically stable.

We observed a similar trend with the XFNTR data where the increase in adsorbed ion density for 20 and 30 mN/m is minimal. Both profiles also show a lower-density region around $Z = 10$ Å, i.e. closer to air. In the less-compressed 20 mN/m, this region has an electron density of $0.061 e^-/\text{Å}^3$ and a thickness of 16.3 Å. The 30 mN/m sample gives an electron density of $0.030 e^-/\text{Å}^3$ with a larger thickness of 21.4 Å. We linked the roughness of all interfaces, as the interfacial roughness is dominated by capillary waves,⁶²⁻⁶³ and found a roughness of 4.32 and 4.47 Å for 20 and 30 mN/m, respectively. We speculate this thicker slab represents tilted GO flakes within the crumpled, multi-layer GO film (Figure 4C). A tilt of even a few degrees can increase the effective length of the micron-size GO flakes thus increasing the total layer thickness. The changes in electron density and slab thickness are more pronounced in between the two considered surface pressures. Because these parameters intrinsically covary,⁷⁶ fits with more similar electron densities and thickness are likely also possible. However, we note that GO is not a typical amphiphilic monolayer and that the overall observed structural differences for 20 and 30 mN/m are minimal.

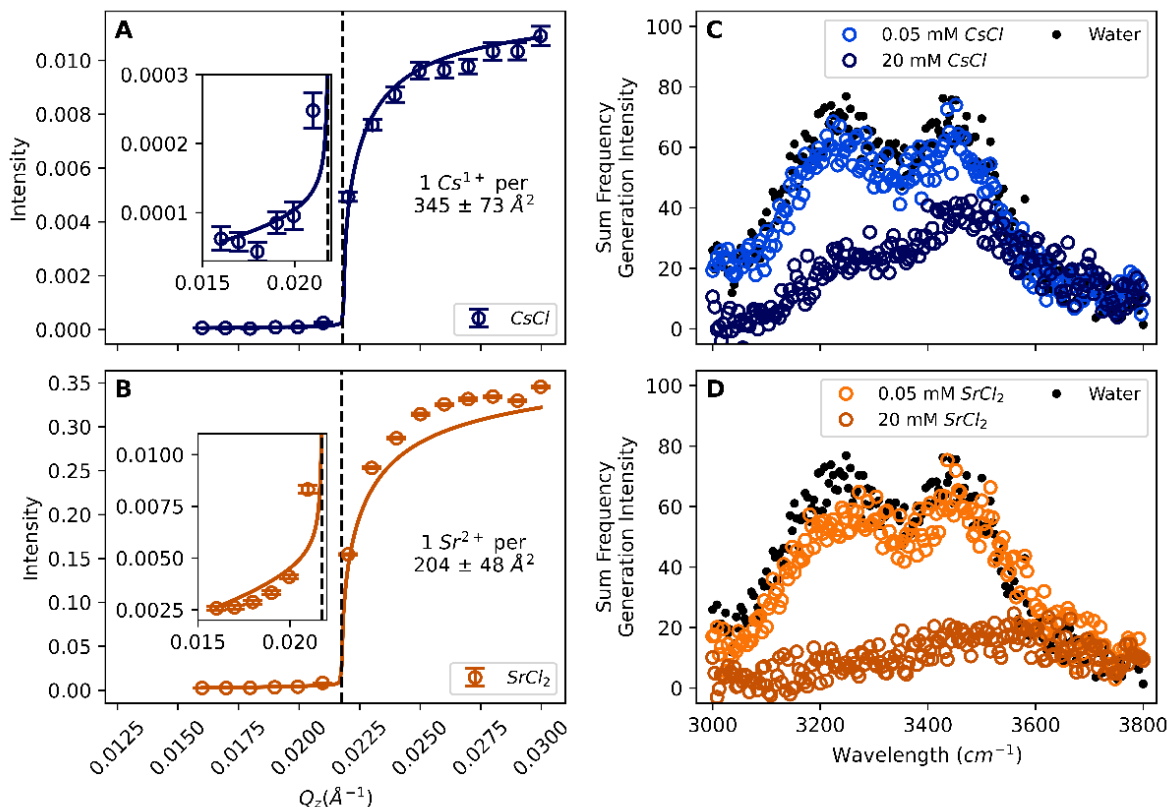


Figure 5. Surface-sensitive x-ray fluorescence near total reflection (XFNTR) intensity and fits (lines) plotted over inverse momentum Q_z for graphene oxide films compressed to 20 mN/m and spread on 20 mM CsCl (A) and SrCl_2 (B) subphases. Error bars are derived from counting statistics. Sum frequency generation spectroscopy intensity plotted over wavelength for the water region of a graphene oxide film compressed to 20 mN/m and spread over concentrated 20 mM (dark colors) and dilute 0.05 mM (light colors) subphases for CsCl (C) and SrCl_2 (D). Typical water band signal is also shown (black).

Mono- and divalent ion adsorption to graphene oxide

As a comparison, we also consider mono- and divalent ion adsorption to GO films at the air-liquid interface. We measured XFNTR for GO samples spread on high concentration 20 mM CsCl and SrCl_2 subphases (Figure 5A-B). For a GO sample compressed to 20 mN/m, we find 1 adsorbed

Cs^{1+} per $345 \pm 73 \text{ \AA}^2$ and 1 adsorbed Sr^{2+} per $204 \pm 48 \text{ \AA}^2$. XFNTTR measured on 0.05 mM CsCl and SrCl_2 subphases (not shown) showed no signal, meaning no ions adsorbed within the detection limit, which is typically 1 ion per $50,000 \text{ \AA}^2$.⁷⁷

To examine molecular water and ion behavior, we used SFG spectroscopy of the -OH stretch of the water region for GO samples compressed to 20 mN/m and spread over dilute and concentrated subphases (Figure 5C-D). SFG data for GO on 0.05 mM CsCl are nearly identical to GO on plain water. This means nearly no Cs^{1+} adsorb to the GO, which is consistent with our XFNTTR results. The 20 mM CsCl data show an intensity decrease in both water bands, indicative of disruption to the well-ordered hydrogen-bonded water network near the interface and indirect evidence of ion adsorption. Given the ion adsorption information obtained from the XFNTTR analysis, we reasonably posit for a 20 mM subphase, some Cs^{1+} adsorbs. We see similar behavior for the 20 and 0.05 mM SrCl_2 SFG data. In this case, the water peak intensity decreases more for the 20 mM subphase – consistent with a higher adsorbed ion density. Taken together, these XFNTTR and SFG data show minimal ion adsorption for both Cs^{1+} and Sr^{2+} . Previous works have demonstrated weak bonding interactions between Cs and bulk GO²³⁻²⁵ with Cs primarily interacting with hydroxyl, epoxy, and sulfur contaminations.²⁵ Bulk studies utilizing Sr^{2+} and GO have also found metal interactions with C-O-C and O-C=O, as well as sulfur contaminates^{23, 26} although the specific adsorption mechanisms are unclear. Evidentially, Y^{3+} adsorbs preferentially to GO compared to both Cs^{1+} and Sr^{2+} .

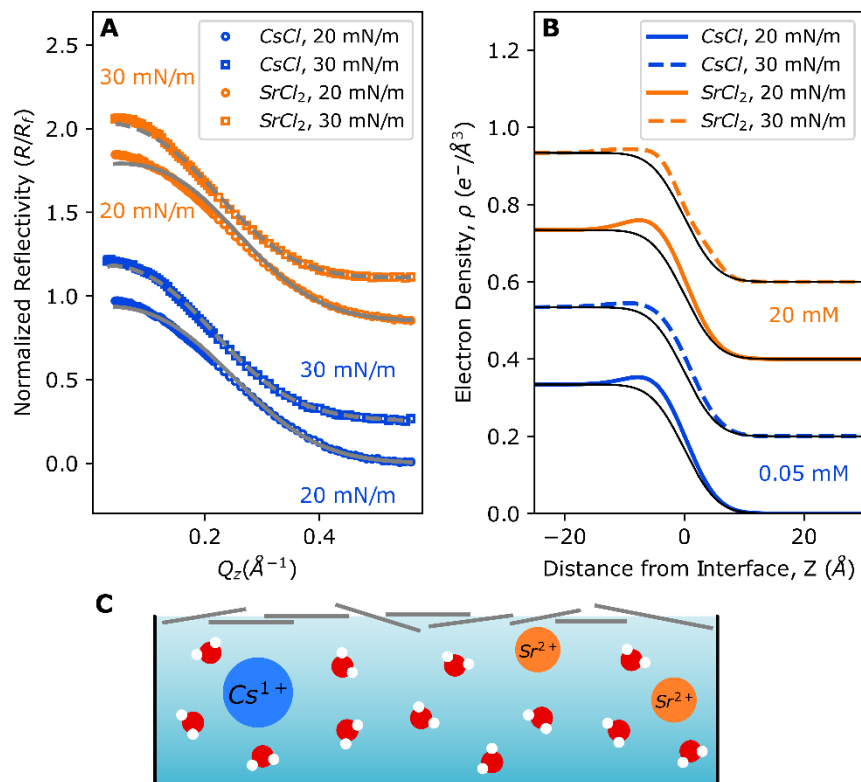


Figure 6. Normalized x-ray reflectivity plotted over vertical momentum transfer, Q_z , for graphene oxide films compressed to 20 (circles) and 30 (squares) mN/m spread on 0.05 mM CsCl (blue) and 20 mM SrCl₂ (orange) subphases. Data were fit using a 1 slab models (lines). Data are vertically offset for clarity. Calculated electron density from fitted reflectivity data plotted over distance from interface Z (B) for graphene oxide monolayers compressed to 20 (solid line) and 30 (dashed line) mN/m spread on 0.05 mM YCl₃ subphases on 0.05 mM CsCl (blue) and 20 mM SrCl₂ (orange) subphases. An ideal interface electron density profile is included (black). Data are vertically offset for clarity. Proposed interfacial structure (not to scale) (C).

We analyzed the GO interfacial structure for samples spread on CsCl and SrCl₂ subphases using XR (Figure 6A). For GO spread on 0.05 mM CsCl, the XR data is nearly featureless with little difference for compression to 20 and 30 mN/m. The slight increase in reflectivity for the 30 mN/m sample is consistent with more GO material within the probed interfacial region, which can then

reflect more signal. We fit these XR data using 1 slab to generate an electron density profile (Figure 6B). These XR data lack distinguishable features, and the absolute slab thickness and electron density parameters are not perfectly reliable, because these parameters intrinsically covary.⁷⁶ However, the EDP generated from the combination of these parameters show little variance.

The 20 mN/m data yield an electron density of $0.41\ e^-/\text{\AA}^3$, a thickness of 6.8 \AA , and a subphase-linked roughness of 4.25 \AA while the 30 mN/m data provide electron density of $4.9\ e^-/\text{\AA}^2$, a thickness of 14.1 \AA , and a subphase-linked roughness of 4.04 \AA . We note the resolution of these XR measurements is $\sim 5.6\ \text{\AA}$. Given our XFNTTR and SFG analysis, we reasonably posit that the XR data show GO flakes assembled at the interface with nearly no adsorbed metal ion interference. The 20 mN/m case, then, likely shows a layer of partially hydrated GO, consistent with other XR measurements,⁴⁹ while the 30 mN/m case shows a more crumpled GO structure, as the electron density and thickness both increase. We posit the increase in surface pressure forces the GO flakes to tilt and create a thicker film. Compared to the Y^{3+} XR data, we speculate the Y^{3+} data reveal a complex interfacial structure with both increased electron density and layer thickness due to the adsorbed ions. These Y^{3+} ions disrupt clear layering, as also observed by others using neat water,⁴⁹ and create a complicated multilayer structure containing GO flakes, adsorbed Y^{3+} , and water.

To understand the GO structure in a partial adsorption case, we measured XR for GO on 20 mM SrCl_2 (Figure 6A). Interestingly, the XR data are again nearly featureless except for the small increase in electron density for the 30 mN/m data, consistent with more scattering materials existing in the probed region. Fitting via a 1 slab model provided an electron density of $0.43\ e^-/\text{\AA}^3$, a thickness of 7.0 \AA , and a roughness of 4.3 \AA for 20 mN/m while the 30 mN/m data yielded an electron density of $0.35\ e^-/\text{\AA}^3$, a thickness of 15.2 \AA , and a roughness of 4.1 \AA . Despite the adsorbed Sr^{2+} ions, as confirmed directly with XFNTTR and indirectly with SFG, the GO structure does not

significantly change compared to the no adsorption case. Again, we speculate the slab in the 20 mN/m system represents a layer of partially hydrated GO, and the slab in the 30 mN/m systems describes a crumpled GO film created from tilted GO flakes. These data support our assertion that Y^{3+} adsorption shows a significant GO structural change. Cs^{1+} and Sr^{2+} ions are likely too facile to significantly adsorb or induce such a rearrangement. These lower valency ions may also be better shielded due to their larger sizes by surrounding anions in solution thus diminishing adsorption capabilities.

CONCLUSIONS

GO is a promising material for separation membranes and sorbents as it combines the robustness of graphene with chemically active functional groups. Despite the usefulness of GO in these systems, little is known about the molecular-scale details of the metal adsorption on GO films. We present XR, XFNTR, and SFG data considering metal ion adsorption onto interfacial thin GO films. These interface-specific techniques provide the total electron density normal to the interface, the quantitative adsorbed ion density, and information about the local water network, respectively. Our XFNTR and SFG data shown that trivalent Y^{3+} adsorbs more strongly even in lower concentrations compared to divalent Sr^{2+} and monovalent Cs^{1+} ions. The XR data show a complex thin film GO structure after Y^{3+} adsorption compared to the no adsorption (0.05 mM CsCl) and minimal ion adsorption (20 mM $SrCl^{2+}$) cases, as confirmed with both XFNTR and SFG. We posit Y^{3+} can cause the GO flakes to tilt and crumple by attracting the hydrophilic flake edges with its significant charge density. Cs^{1+} and Sr^{2+} are likely too facile to induce such a change and may have reduced effective charges due to local anion shielding.

Additionally, we present for the first time SFG data demonstrating trivalent ion adsorption onto interfacial GO films. Our SFG analysis shows a significant change in the local interfacial

water network upon adsorption of Y^{3+} on the GO film, evidenced by the decrease in water region signal. We attribute the observed 3400 cm^{-1} to weakly hydrogen bound water molecules near the GO film or in between the crumpled GO layers. Interestingly, the intensity of this band is nearly independent of subphase concentration, which suggests these water molecules remain unaffected until the total water network is significantly disrupted. These interfacial-specific techniques provide important molecular information about ion adsorption and supporting future studies of GO for soft-scaffold applications.

ASSOCIATED CONTENT

Supporting Information. Graphene oxide monolayer characterization, x-ray fluorescence near total reflection on high concentration yttrium subphase at 30 mN/m data, vibrational sum frequency spectroscopy fitting parameters.

AUTHOR INFORMATION

Corresponding Author

* Ahmet Uysal, Email: ahmet@anl.gov, Web: <https://www.anl.gov/profile/ahmet-uysal>

Author Contributions

The manuscript was written through contributions of all authors. All authors have given approval to the final version of the manuscript.

ACKNOWLEDGMENT

This material is based upon work supported by the U.S. Department of Energy, Office of Basic Energy Science, Division of Chemical Sciences, Geosciences, and Biosciences, Early Career Research Program under contract DE-AC02-06CH11357. Use of the Advanced Photon Source and

the Center for Nanoscale Materials, both Office of Science User Facilities operated for the U.S. Department of Energy (DOE), Office of Science by Argonne National Laboratory, was supported by the U.S. DOE under Contract no. DE-AC02-06CH11357. NSF's ChemMatCARS Sector 15 is supported by the Divisions of Chemistry (CHE) and Materials Research (DMR), National Science Foundation, under Grant NSF/CHE-1834750. This work made use of the Keck-II facility of Northwestern University's NUANCE Center, which has received support from the SHyNE Resource (NSF ECCS-2025633), the IIN, and Northwestern's MRSEC program (NSF DMR-1720139).

REFERENCES

1. Liu, G.; Jin, W.; Xu, N. Graphene-based membranes. *Chem. Soc. Rev.* **2015**, *44*, 5016-30.
2. Rowley-Neale, S. J.; Randviir, E. P.; Abo Dena, A. S.; Banks, C. E. An overview of recent applications of reduced graphene oxide as a basis of electroanalytical sensing platforms. *Appl. Mater. Today* **2018**, *10*, 218-226.
3. Lurf, A.; He, H.; Forster, M.; Klinowski, J. Structure of Graphite Oxide Revisited. *J. Phys. Chem. B* **1998**, *102*, 4477-4482.
4. Liu, S.; Hu, K.; Cerruti, M.; Barthelat, F. Ultra-stiff graphene oxide paper prepared by directed-flow vacuum filtration. *Carbon* **2020**, *158*, 426-434.
5. Bullock, C. J.; Bussy, C. Biocompatibility Considerations in the Design of Graphene Biomedical Materials. *Adv. Mater. Interfaces* **2019**.
6. Cote, L. J.; Kim, F.; Huang, J. Langmuir–Blodgett Assembly of Graphite Oxide Single Layers. *Journal of the American Chemical Society* **2009**, *131*, 1043-1049.

7. Kim, J.; Cote, L. J.; Kim, F.; Yuan, W.; Shull, K. R.; Huang, J. Graphene oxide sheets at interfaces. *J. Am. Chem. Soc.* **2010**, *132*, 8180-6.
8. Lopez-Diaz, D.; Merchan, M. D.; Velazquez, M. M. The behavior of graphene oxide trapped at the air water interface. *Adv. Colloid Interface Sci.* **2020**, *286*, 102312.
9. Sheka, E. F.; Natkaniec, I. Neutron scattering of parent and reduced graphene oxide. *Rev. Adv. Mater. Sci.* **2017**, *49*, 1-27.
10. Coleman, B. R.; Knight, T.; Gies, V.; Jakubek, Z. J.; Zou, S. Manipulation and Quantification of Graphene Oxide Flake Size: Photoluminescence and Cytotoxicity. *ACS Appl. Mater. Interfaces* **2017**, *9*, 28911-28921.
11. Chen, J.; Chi, F.; Huang, L.; Zhang, M.; Yao, B.; Li, Y.; Li, C.; Shi, G. Synthesis of graphene oxide sheets with controlled sizes from sieved graphite flakes. *Carbon* **2016**, *110*, 34-40.
12. Krishnamoorthy, K.; Veerapandian, M.; Yun, K.; Kim, S. J. The chemical and structural analysis of graphene oxide with different degrees of oxidation. *Carbon* **2013**, *53*, 38-49.
13. Kim, H. W.; Yoon, H. W.; Yoon, S. M.; Yoo, B. M.; Ahn, B. K.; Cho, Y. H.; Shin, H. J.; Yang, H.; Paik, U.; Kwon, S.; Choi, J. Y.; Park, H. B. Selective gas transport through few-layered graphene and graphene oxide membranes. *Science* **2013**, *342*, 91-5.
14. Joshi, R. K.; Carbone, P.; Wang, F. C.; Kravets, V. G.; Su, Y.; Grigorieva, I. V.; Wu, H. A.; Geim, A. K.; Nair, R. R. Precise and ultrafast molecular sieving through graphene oxide membranes. *Science* **2014**, *343*, 752-4.
15. Mi, B. Graphene oxide membranes for ionic and molecular sieving. *Science* **2014**, *343*, 740-2.

16. Nair, R. R.; Wu, H. A.; Jayaram, P. N.; Grigorieva, I. V.; Geim, A. K. Unimpeded permeation of water through helium-leak-tight graphene-based membranes. *Science* **2012**, *335*, 442-4.
17. Hu, M.; Mi, B. Enabling graphene oxide nanosheets as water separation membranes. *Environ. Sci. Technol.* **2013**, *47*, 3715-23.
18. Romaniak, G.; Dybowski, K.; Jeziorna, A.; Kula, P.; Kaźmierczak, T. Synthesis and characterization of semi-permeable graphene/graphene oxide membranes for water desalination. *J. Mater. Sci.* **2020**, *55*, 9775-9786.
19. Sun, P.; Zhu, M.; Wang, K.; Zhong, M.; Wei, J.; Wu, D.; Xu, Z.; Zhu, H. Selective ion penetration of graphene oxide membranes. *ACS Nano* **2013**, *7*, 428-37.
20. Liu, R.; Arabale, G.; Kim, J.; Sun, K.; Lee, Y.; Ryu, C.; Lee, C. Graphene oxide membrane for liquid phase organic molecular separation. *Carbon* **2014**, *77*, 933-938.
21. Yang, S.; Chen, X.; Zhang, Z.; Jin, P.; Zhang, Q.; Wang, X. The Removal of Phosphate from Aqueous Solution through Chemical Filtration Using a Sponge Filter. *Chem. Lett.* **2018**, *47*, 89-91.
22. Hu, M.; Zheng, S.; Mi, B. Organic Fouling of Graphene Oxide Membranes and Its Implications for Membrane Fouling Control in Engineered Osmosis. *Environ. Sci. Technol.* **2016**, *50*, 685-93.
23. Romanchuk, A. Y.; Kuzenkova, A. S.; Slesarev, A. S.; Tour, J. M.; Kalmykov, S. N. Cs(I) and Sr(II) Sorption onto Graphene Oxide. *Solvent Extr. Ion Exch.* **2016**, *34*, 594-602.

24. Kaewmee, P.; Manyam, J.; Opaprakasit, P.; Truc Le, G. T.; Chanlek, N.; Sreearunothai, P. Effective removal of cesium by pristine graphene oxide: performance, characterizations and mechanisms. *RSC Advances* **2017**, *7*, 38747-38756.
25. Kuzenkova, A. S.; Romanchuk, A. Y.; Trigub, A. L.; Maslakov, K. I.; Egorov, A. V.; Amidani, L.; Kittrell, C.; Kvashnina, K. O.; Tour, J. M.; Talyzin, A. V.; Kalmykov, S. N. New insights into the mechanism of graphene oxide and radionuclide interaction. *Carbon* **2020**, *158*, 291-302.
26. Xing, M.; Zhuang, S.; Wang, J. Adsorptive removal of strontium ions from aqueous solution by graphene oxide. *Environ. Sci. Pollut. Res. Int.* **2019**, *26*, 29669-29678.
27. Romanchuk, A. Y.; Slesarev, A. S.; Kalmykov, S. N.; Kosynkin, D. V.; Tour, J. M. Graphene oxide for effective radionuclide removal. *Phys. Chem. Chem. Phys.* **2013**, *15*, 2321-7.
28. Nguyen, M. T.; Zhang, J.; Prabhakaran, V.; Tan, S.; Baxter, E. T.; Shutthanandan, V.; Johnson, G. E.; Rousseau, R.; Glezakou, V. A. Graphene Oxide as a Pb(II) Separation Medium: Has Part of the Story Been Overlooked? *JACS Au* **2021**, *1*, 766-776.
29. Xie, Y.; Helvenston, E. M.; Shuller-Nickles, L. C.; Powell, B. A. Surface Complexation Modeling of Eu(III) and U(VI) Interactions with Graphene Oxide. *Environ. Sci. Technol.* **2016**, *50*, 1821-7.
30. Hu, B.; Hu, Q.; Li, X.; Pan, H.; Tang, X.; Chen, C.; Huang, C. Rapid and highly efficient removal of Eu(III) from aqueous solutions using graphene oxide. *J. Mol. Liq.* **2017**, *229*, 6-14.
31. Boulanger, N.; Kuzenkova, A. S.; Iakunkov, A.; Romanchuk, A. Y.; Trigub, A. L.; Egorov, A. V.; Bauters, S.; Amidani, L.; Retegan, M.; Kvashnina, K. O.; Kalmykov, S. N.; Talyzin, A. V.

Enhanced Sorption of Radionuclides by Defect-Rich Graphene Oxide. *ACS Appl. Mater. Interfaces* **2020**, *12*, 45122-45135.

32. Xie, Y.; Powell, B. A. Linear Free Energy Relationship for Actinide Sorption to Graphene Oxide. *ACS Appl. Mater. Interfaces* **2018**, *10*, 32086-32092.

33. Bai, Z.-Q.; Li, Z.-J.; Wang, C.-Z.; Yuan, L.-Y.; Liu, Z.-R.; Zhang, J.; Zheng, L.-R.; Zhao, Y.-L.; Chai, Z.-F.; Shi, W.-Q. Interactions between Th(IV) and graphene oxide: experimental and density functional theoretical investigations. *RSC Adv.* **2014**, *4*, 3340-3347.

34. Mohamud, H.; Ivanov, P.; Russell, B. C.; Regan, P. H.; Ward, N. I. Selective sorption of uranium from aqueous solution by graphene oxide-modified materials. *J. Radioanal. Nucl. Chem.* **2018**, *316*, 839-848.

35. Zhao, D.; Gao, X.; Chen, S.; Xie, F.; Feng, S.; Alsaedi, A.; Hayat, T.; Chen, C. Interaction between U(VI) with sulfhydryl groups functionalized graphene oxides investigated by batch and spectroscopic techniques. *J. Colloid Interface Sci.* **2018**, *524*, 129-138.

36. Yang, P.; Zhang, H.; Liu, Q.; Liu, J.; Chen, R.; Yu, J.; Hou, J.; Bai, X.; Wang, J. Nano-sized architectural design of multi-activity graphene oxide (GO) by chemical post-decoration for efficient uranium(VI) extraction. *J. Hazard. Mater.* **2019**, *375*, 320-329.

37. Wu, M.; Kempaiah, R.; Huang, P. J.; Maheshwari, V.; Liu, J. Adsorption and desorption of DNA on graphene oxide studied by fluorescently labeled oligonucleotides. *Langmuir* **2011**, *27*, 2731-8.

38. Chang, K.; Sun, Y.; Ye, F.; Li, X.; Sheng, G.; Zhao, D.; Linghu, W.; Li, H.; Liu, J. Macroscopic and molecular study of the sorption and co-sorption of graphene oxide and Eu(III) onto layered double hydroxides. *Chem. Eng. J.* **2017**, *325*, 665-671.
39. Mandal, P.; Bhattacharya, G.; Bhattacharyya, A.; Roy, S. S.; Ghosh, S. K. Unravelling the structural changes of phospholipid membranes in presence of graphene oxide. *Appl. Surf. Sci.* **2021**, *539*.
40. Bliznyuk, V. N.; Conroy, N. A.; Xie, Y.; Podila, R.; Rao, A. M.; Powell, B. A. Increase in the reduction potential of uranyl upon interaction with graphene oxide surfaces. *Phys. Chem. Chem. Phys.* **2018**, *20*, 1752-1760.
41. Barker, D.; Fors, A.; Lindgren, E.; Olesund, A.; Schroder, E. Filter function of graphene oxide: Trapping perfluorinated molecules. *J. Chem. Phys.* **2020**, *152*, 024704.
42. Gravelle, S.; Botto, L. Adsorption of Single and Multiple Graphene-Oxide Nanoparticles at a Water-Vapor Interface. *Langmuir* **2021**, *37*, 13322-13330.
43. Sutar, D. S.; Narayanam, P. K.; Singh, G.; Botcha, V. D.; Talwar, S. S.; Srinivasa, R. S.; Major, S. S. Spectroscopic studies of large sheets of graphene oxide and reduced graphene oxide monolayers prepared by Langmuir–Blodgett technique. *Thin Solid Films* **2012**, *520*, 5991-5996.
44. Cote, L. J.; Kim, F.; Huang, J. Langmuir-Blodgett assembly of graphite oxide single layers. *J. Am. Chem. Soc.* **2009**, *131*, 1043-9.
45. Bramhaiah, K.; John, N. S. Facile synthesis of reduced graphene oxide films at the air–water interface and in situ loading of noble metal nanoparticles. *Adv. Nat. Sci.: Nanosci. Nanotechnol.* **2012**, *3*.

46. Hidalgo, R. S.; Lopez-Diaz, D.; Velazquez, M. M. Graphene oxide thin films: influence of chemical structure and deposition methodology. *Langmuir* **2015**, *31*, 2697-705.
47. Turpin, G. A.; Holt, S. A.; Scofield, J. M. P.; Teo, B. M.; Tabor, R. F. Spontaneous Adsorption of Graphene Oxide to Oil–Water and Air–Water Interfaces by Adsorption of Hydrotropes. *Adv. Mater. Interfaces* **2020**, *7*.
48. Fang, S.; Chen, T.; Chen, B.; Xiong, Y.; Zhu, Y.; Duan, M. Graphene oxide at oil-water interfaces: Adsorption, assembly & demulsification. *Colloids Surf., A* **2016**, *511*, 47-54.
49. Bonatout, N.; Muller, F.; Fontaine, P.; Gascon, I.; Konovalov, O.; Goldmann, M. How exfoliated graphene oxide nanosheets organize at the water interface: evidence for a spontaneous bilayer self-assembly. *Nanoscale* **2017**, *9*, 12543-12548.
50. David, R.; Tuladhar, A.; Zhang, L.; Arges, C.; Kumar, R. Effect of Oxidation Level on the Interfacial Water at the Graphene Oxide-Water Interface: From Spectroscopic Signatures to Hydrogen-Bonding Environment. *J. Phys. Chem. B* **2020**, *124*, 8167-8178.
51. Ishiyama, T.; Imamura, T.; Morita, A. Theoretical studies of structures and vibrational sum frequency generation spectra at aqueous interfaces. *Chem. Rev.* **2014**, *114*, 8447-8470.
52. Geiger, F. M. Second harmonic generation, sum frequency generation, and $\chi(3)$: dissecting environmental interfaces with a nonlinear optical Swiss Army knife. *Annu. Rev. Phys. Chem.* **2009**, *60*, 61-83.
53. Zhang, Z.; Kim, J.; Khoury, R.; Saghaezyan, M.; Haber, L. H.; Plummer, E. Surface sum frequency generation spectroscopy on non-centrosymmetric crystal GaAs (001). *Surf. Sci.* **2017**, *664*, 21-28.

54. David, R.; Kumar, R. Reactive events at the graphene oxide-water interface. *Chem. Commun.* **2021**, *57*, 11697-11700.
55. Lovering, K.; Nayak, S.; Bu, W.; Uysal, A. The Role of Specific Ion Effects in Ion Transport: The Case of Nitrate and Thiocyanate. *J. Phys. Chem. C* **2019**, *124*, 573-581.
56. Rock, W.; Qiao, B.; Zhou, T.; Clark, A. E.; Uysal, A. Heavy Anionic Complex Creates a Unique Water Structure at a Soft Charged Interface. *J. Phys. Chem. C* **2018**, *122*, 29228-29236.
57. Nayak, S.; Kumal, R. R.; Liu, Z.; Qiao, B.; Clark, A.; Uysal, A. Origins of Clustering of Metalate-Extractant Complexes in Liquid-Liquid Extraction. *ACS Appl. Mater. Interfaces* **2021**, *13*, 24194-24206.
58. Kumal, R.; Nayak, S.; Bu, W.; Uysal, A. Chemical Potential Driven Reorganization of Anions between Stern and Diffuse Layers at the Air/Water Interface. *J. Phys. Chem. C* **2022**, *126*, 1140-1151.
59. Ohno, P. E.; Wang, H.-f.; Geiger, F. M. Second-order spectral lineshapes from charged interfaces. *Nat. Commun.* **2017**, *8*, 1-9.
60. Wen, Y.-C.; Zha, S.; Liu, X.; Yang, S.; Guo, P.; Shi, G.; Fang, H.; Shen, Y. R.; Tian, C. Unveiling microscopic structures of charged water interfaces by surface-specific vibrational spectroscopy. *Phys. Rev. Lett.* **2016**, *116*, 016101-016105.
61. Kumal, R. R.; Karam, T. E.; Haber, L. H. Determination of the surface charge density of colloidal gold nanoparticles using second harmonic generation. *J. Phys. Chem. C* **2015**, *119*, 16200-16207.

62. Bera, M. K.; Bu, W.; Uysal, A. Liquid surface x-ray scattering. In *Physical Chemistry of Gas-Liquid Interfaces*, Faust, J.; House, J., Eds. Elsevier: 2018; pp 167-194.
63. Danauskas, S. M.; Li, D.; Meron, M.; Lin, B.; Lee, K. Y. C. Stochastic fitting of specular X-ray reflectivity data using StochFit. *J. Appl. Crystallogr.* **2008**, *41*, 1187-1193.
64. Thompson, A.; Attwood, D.; Gullikson, E.; Howells, M.; Kim, K.-J.; Kirz, J.; Kortright, J.; Lindau, I.; Lu, Y.; Pianetta, P.; Robinson, A.; Scofield, J.; Underwood, J.; Williams, G.; Winick, H. *X-ray Data Booklet*. 3 ed.; Lawrence Berkeley National Lab: Berkeley, CA, 2009.
65. Bu, W.; Mihaylov, M.; Amoanu, D.; Lin, B.; Meron, M.; Kuzmenko, I.; Soderholm, L.; Schlossman, M. L. X-ray Studies of Interfacial Strontium–Extractant Complexes in a Model Solvent Extraction System. *J. Phys. Chem. B* **2014**, *118*, 12486-12500.
66. Nayak, S.; Lovering, K.; Bu, W.; Uysal, A. Anions Enhance Rare Earth Adsorption at Negatively Charged Surfaces. *J. Phys. Chem. Lett.* **2020**, *11*, 4436-4442.
67. Carr, A. J.; Lee, S. S.; Uysal, A. Trivalent ion overcharging on electrified graphene. *J. Phys.: Condens. Matter* **2022**, *34*, 144001.
68. Tuladhar, A.; Piontek, S. M.; Frazer, L.; Borguet, E. Effect of Halide Anions on the Structure and Dynamics of Water Next to an Alumina (0001) Surface. *J. Phys. Chem. C* **2018**, *122*, 12819-12830.
69. Jena, K. C.; Covert, P. A.; Hore, D. K. The Effect of Salt on the Water Structure at a Charged Solid Surface: Differentiating Second- and Third-order Nonlinear Contributions. *J. Phys. Chem. Lett.* **2011**, *2*, 1056-1061.

70. Ma, G.; Chen, X.; Allen, H. C. Dangling OD Confined in a Langmuir Monolayer. *Journal of the American Chemical Society* **2007**, *129*, 14053-14057.
71. Eigler, S.; Dotzer, C.; Hof, F.; Bauer, W.; Hirsch, A. Sulfur species in graphene oxide. *Chem. Eur. J.* **2013**, *19*, 9490-6.
72. Sung, W.; Wang, W.; Lee, J.; Vaknin, D.; Kim, D. Specificity and Variation of Length Scale over Which Monovalent Halide Ions Neutralize a Charged Interface. *J. Phys. Chem. C* **2015**, *119*, 7130-7137.
73. Sthoer, A.; Adams, E. M.; Sengupta, S.; Corkery, R. W.; Allen, H. C.; Tyrode, E. C. La³⁺ and Y³⁺ interactions with the carboxylic acid moiety at the liquid/vapor interface: Identification of binding complexes, charge reversal, and detection limits. *J. Colloid Interface Sci.* **2022**, *608*, 2169-2180.
74. Hong, Y.; He, J.; Zhang, C.; Wang, X. Probing the Structure of Water at the Interface with Graphene Oxide Using Sum Frequency Generation Vibrational Spectroscopy. *J. Phys. Chem. C* **2022**.
75. Uysal, A.; Rock, W.; Qiao, B.; Bu, W.; Lin, B. Two-Step Adsorption of PtCl₆²⁻ Complexes at a Charged Langmuir Monolayer: Role of Hydration and Ion Correlations. *J. Phys. Chem. C* **2017**, *121*, 25377-25383.
76. Uysal, A.; Chu, M.; Stripe, B.; Timalina, A.; Chattopadhyay, S.; Schlepütz, C. M.; Marks, T. J.; Dutta, P. What x rays can tell us about the interfacial profile of water near hydrophobic surfaces. *Phys. Rev. B* **2013**, *88*, 035431.

77. Sun, P.; Binter, E. A.; Liang, Z.; Brown, M. A.; Gelis, A. V.; Benjamin, I.; Bera, M. K.; Lin, B.; Bu, W.; Schlossman, M. L. Antagonistic Role of Aqueous Complexation in the Solvent Extraction and Separation of Rare Earth Ions. *ACS Cent. Sci.* **2021**, 7, 1908-1918.